Microelectronic Engineering 302 (2026) 112426

Contents lists available at ScienceDirect

Microelectronic Engineering

journal homepage: www.elsevier.com/locate/mee

Research paper

Simulation of SAF-enhanced multilayered STT-MRAM structures☆

M. Bendra [a,b,*], W. Goes [c], S. Selberherr [b], V. Sverdlov [a,b]

[a] Christian Doppler Laboratory for Nonvolatile Magnetoresistive Memory and Logic at the Institute for Microelectronics, TU Wien, Gußhausstraße 27-29, Wien, A-1040, Austria
[b] Institute for Microelectronics, TU Wien, Gußhausstraße 27-29, Wien, A-1040, Austria
[c] Silvaco Europe Ltd., Compass Point, St Ives, Cambridge, PE27 5JL, United Kingdom

ARTICLE INFO

Keywords:
STT-MRAM
Synthetic antiferromagnets
Interlayer exchange coupling
Magnetic stability

ABSTRACT

The reliability of multilayered spin-transfer torque magnetoresistive random access memory with synthetic antiferromagnets is crucial for computing-in-memory architectures, high-performance computing, and high-density storage applications. This study investigates the role of interlayer exchange coupling in magnetic tunnel junction structures, which are fundamental to spin-transfer torque magnetoresistive random access memory performance and stability. We analyze how interlayer exchange coupling influences magnetic stability and spin-transfer torque switching efficiency using finite element method simulations combined with the Landau–Lifshitz–Gilbert equation. Our findings reveal that optimizing interlayer exchange coupling not only enhances data retention and write/read speeds but also mitigates miniaturization challenges and improves device reliability in downscaled spin-transfer torque magnetoresistive random access memory technologies. The results further emphasize the strong dependence of interlayer exchange coupling on spacer properties, which dictate magnetic orientations and coupling energy, offering a strategic pathway to engineer more efficient and robust spin-transfer torque magnetoresistive random access memory devices. This work highlights the critical impact of magnetic coupling on the switching dynamics and long-term stability of spintronic memory, providing insights that pave the way for next-generation, high-performance memory solutions.

1. Introduction

Investigating the reliability of multilayered spin-transfer torque magnetoresistive random access memory (STT-MRAM) equipped with synthetic antiferromagnets (SAF) is paramount, especially as this technology finds increasing application in sectors such as computing-in-memory systems [1–3], automotive [4], neural systems [5], real-time industrial environments [6], high-performance computing [7], system-level energy-efficient logic [3], neuromorphic computing [8], and high-density storage configurations [9]. Central to STT-MRAM's architecture is the magnetic tunnel junction (MTJ), consisting of a CoFeB reference layer (RL) and a free layer (FL), separated by an MgO tunnel barrier (TB) or a non-magnetic spacer (NMS), a design critical for achieving the miniaturization necessary for high-density memory advancements [10,11].

This work extends our previous findings, incorporating additional analyses and a more comprehensive investigation into the role of interlayer exchange coupling (IEC) in STT-MRAM performance [12].

The trend towards smaller cell sizes, however, introduces significant reliability challenges, including the back-hopping phenomenon, which compromises memory cell stability [13,14]. Addressing these issues has led to a concentrated effort on leveraging IEC, a mechanism vital for the performance and stability of memory cells, particularly in multi-layer cell configurations and complex MTJ stacks aimed at increasing memory density [15].

IEC's role in defining the magnetic orientation of ferromagnetic layers, with a focus on the efficiency of metallic spacers, has been extensively studied to adapt MTJ performance across a wide array of applications, potentially replacing traditional memory systems like SRAM, DRAM, and flash memory [16–18]. Advancements in MTJ technology, especially in the CoFeB/MgO system known for its perpendicular magnetic anisotropy, include efforts to enhance interfacial anisotropy through strategies like adding a capping layer or inserting additional MgO or non-magnetic spacer layers within the free layer [10,19]. These innovations have facilitated the downscaling of MTJ dimensions and their commercialization by semiconductor foundries [20–22].

Our research explores IEC's effects on magnetic stability and STT switching efficiency in multilayered structures. By optimizing IEC, we aim to enhance data retention and write/read speeds, addressing the

☆ This article is part of a Special issue entitled: AMNDCE published in Microelectronic Engineering.

* Corresponding author at: Institute for Microelectronics, TU Wien, Gußhausstraße 27-29, Wien, A-1040, Austria.
E-mail address: bendra@iue.tuwien.ac.at (M. Bendra).

https://doi.org/10.1016/j.mee.2025.112426
Received 5 February 2025; Received in revised form 17 September 2025; Accepted 29 October 2025
Available online 6 November 2025

reliability challenges of STT-MRAM. Our work supports the development of next-generation memory systems and their integration into mainstream applications.

2. Micromagnetic simulation

We use the finite element method (FEM) to model magnetization dynamics, applying the Landau–Lifshitz–Gilbert (LLG) equation, which is expressed as:

$$\frac{\partial \mathbf{m}}{\partial t} = -\gamma \mathbf{m} \times \mathbf{H}_{\text{eff}} + \alpha \mathbf{m} \times \frac{\partial \mathbf{m}}{\partial t} + \frac{1}{M_S} \mathbf{T}_{\mathbf{S}}. \tag{1}$$

$\mathbf{m}$ represents the normalized magnetization vector, γ denotes the gyromagnetic ratio, and α is the Gilbert damping constant. The term $\mathbf{H}_{\text{eff}}$ denotes the effective field, while $\mathbf{T}_{\mathbf{S}}$ accounts for spin-transfer torque contributions [23].

We solve the LLG dynamics with a backward-Euler (implicit first-order) time integrator using a fixed time step of 0.1 ps. After each time step $\mathbf{m}$ is projected pointwise to unit length. The demagnetizing field is computed with a hybrid finite element-boundary element method open-boundary formulation [24]. The resulting linear systems are nonsymmetric and are solved by GMRES with a block-diagonal preconditioner (relative tolerance 10^{-10}, up to 200 iterations). The coupled spin and charge drift–diffusion equations are likewise solved with GMRES. Interface boundary conditions at the ferromagnet/MgO interfaces follow Fiorentini et al. (spin-current continuity with angle-dependent interface conductances and transverse-spin absorption), which reproduces the voltage and angle dependence of torques in MTJs [23]. The finite-element mesh contains approximately 9,582 elements depending on device size and local refinement. Following [23], the spin-torque term is written explicitly as

$$\mathbf{T}_{\mathbf{S}} = -\frac{D_e}{\lambda_J^2} \mathbf{m} \times \mathbf{S} - \frac{D_e}{\lambda_\varphi^2} \mathbf{m} \times (\mathbf{m} \times \mathbf{S}), \tag{2}$$

where D_e is the electron diffusion constant, $\mathbf{S}$ is the itinerant spin accumulation, and λ_J and λ_φ are the exchange–precession and dephasing lengths.

In multilayer structures, magnetic layers can exhibit exchange coupling even when separated by a nonmagnetic spacer layer. This interaction, initially proposed by Ruderman and Kittel [25], is mediated by conduction electrons in the spacer. The coupling constant oscillates as a function of the spacer layer thickness, leading to either ferromagnetic or antiferromagnetic coupling depending on the spacer's thickness. Kasuya [26] and Yosida [27] later extended this concept, formulating what is now known as the Ruderman–Kittel–Kasuya–Yosida (RKKY) interaction.

In the continuum approximation, the interaction is modeled as a coupling between the interfaces of the magnetic and spacer layers, assuming these interfaces are of equal size. The interlayer-exchange energy, denoted by J, varies in magnitude and sign based on the spacer layer thickness.

IEC, essential for MRAM operation, is described by the interlayer coupling energy density:

$$\mathbf{E} = -J \cos(\Delta\phi) \tag{3}$$

$\Delta\phi$ represents the angle between the magnetizations of the coupled layers, and J is the coupling strength. IEC depends on the electronic structure of the spacer, oscillating in metallic spacers while decaying in semiconductors and insulators, thus influencing both the coupling energy and magnetic orientations [25,28].

The RKKY interaction is widely utilized in designing synthetic antiferromagnets, where the spacer layer thickness is chosen such that J is either positive or negative, ensuring ferromagnetic or antiferromagnetic coupling between the magnetic layers. These synthetic antiferromagnets offer high stability and minimal stray fields, making them ideal for spintronic applications.

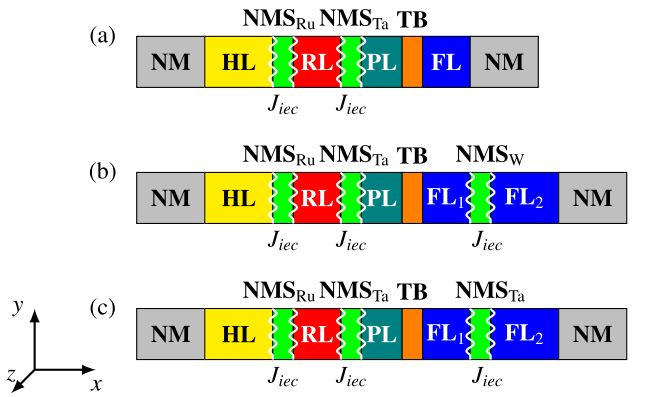

Fig. 1. This figure shows the intricate design of a multilayered MRAM cell. Color-coding is utilized for clear differentiation of components: the hard layer (HL) is marked in yellow, the RL in red, the FL in blue, the PL in teal, the TB in orange, the NMS in green, and the NM contacts are represented in gray. White zigzag lines highlight interfacial engineering regions.

IEC primarily arises from interfacial effects mediated by the spacer, meaning its energy contribution is derived from an interface integral. This coupling directly impacts switching thresholds and stability in STT-MRAM devices [29]. In micromagnetic modeling, these contributions are typically incorporated via boundary conditions. However, representing all energy terms in terms of an effective field rather than with boundary conditions in dynamic micromagnetics is often more convenient for facilitating integration into the LLG equation [28].

For the numerical solution, we use the FEM, implemented in C++ with the open-source MFEM library. The implementation details can be found in [30,31].

Fig. 1(a) depicts a complex MRAM structure incorporating a CoPt hard layer (HL) and a RL, accompanied by Ru and Ta NMS, a CoFeB spin-polarization layer (PL), an MgO TB, and a CoFeB FL. All structures feature a HL, which is AFM-linked with a RL through a Ru NMS$_{Ru}$. Additionally, the RL is connected to the PL via ferromagnetic (FM) coupling through Ta NMS$_{Ta}$. The antiferromagnetic (AFM) coupling facilitated by NMS$_{Ru}$ exhibits a notable coupling force of -1.5 mJ m^{-2} [32], indicative of a robust AFM connection. The dimensions are as follows: HL at 5.3 nm, NMS$_{Ru}$ at 0.85 nm, RL at 3.2 nm, NMS$_{Ta}$ at 0.4 nm, PL at 1.3 nm, TB at 0.9 nm, and FL at 1.4 nm, ending with non-magnetic contacts at 50 nm. To align with experiment, we use RA = 6.5 Ω μm^2 and TMR = 150% because they lie within reported ranges for CoFeB/MgO pMTJs at room temperature (RA ≈ 6–7 Ω μm^2 with TMR ≈ 100%–250%) [33–35]. The 70 nm junction diameter was selected because it is widely used in experimental tests and demonstrations, offering a practical balance between device-to-device variability, thermal stability, and switching-current levels, and it is representative of many published studies that investigate reliability and fast switching in 50–70 nm MTJs [36,37]. We keep the diameter fixed here to isolate the effects. Still, the expected trends with size are well established: at fixed materials and stack, the critical switching current scales approximately with junction area (and thus with D^2) [38]. At the same time, details of the reversal pathway can vary with diameter due to domain-wall-mediated processes reported for 50–250 nm devices [39]. These considerations support our baseline choice (70 nm) and parameterization while providing context for extrapolation to nearby sizes (e.g., 50 or 100 nm).

Fig. 1(b) and 1(c) illustrate variations in the FL in a hybrid configuration. In Fig. 1(b), the FL is separated by a tungsten NMS into CoFeB (FL$_1$) and CoPt (FL$_2$), while in Fig. 1(c), it is separated by a tantalum NMS. The dimensions of the FL are: FL$_1$ at 0.8 nm, NMS at 0.3 nm for both W and Ta spacers, and FL$_2$ at 3.5 nm. The resistance-area product and tunnel magnetoresistance for these structures are RA_P = 19.9 Ω μm^2, TMR 80% for Fig. 1(b), and RA_P = 14.6 Ω μm^2,

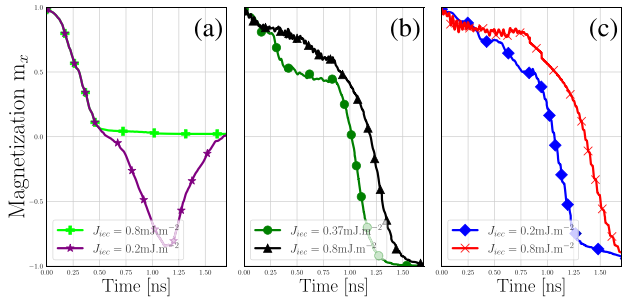

Fig. 2. Switching duration with different FM coupling, (a) for the structure in Fig. 1(a), (b) for the structure in Fig. 1(b), and (c) for the structure in Fig. 1(c).

TMR 80% for Fig. 1(c). The overall diameter for all stacks is 70 nm. The simulation parameters applied across the various MRAM configurations illustrated in Fig. 1, with appropriate references provided in [40–45].

Fig. 2 shows the magnetization trajectories during the transition from parallel (P) to antiparallel (AP) alignments at a 2 V bias for the structures illustrated in Fig. 1. Figs. 3–8 show the P to AP switching sequence and the role of IEC. The *left* panels display the top free layer (FL or FL_2), while the *right* panels display the underlying layers (PL or FL_1). Subpanels (a)–(c) denote, respectively, the initial state, the intermediate phase during reversal, and the final state. This convention makes it straightforward to compare how IEC strength and spacer choice shape the magnetization trajectories across layers.

In Fig. 2(a), the initial magnetization set at $m_x = 1$ represents the average magnetization direction of both the PL and the FL, oriented positively along the x-axis, for the structure in Fig. 1(a). The initial FM connection through NMS_{Ta}, proposed at 0.8 $mJ\,m^{-2}$ by Devolder et al. [41], represents a substantial FM coupling. However, subsequent works by Devolder et al. [42] and Goff et al. [43] revised this FM coupling strength to 0.2 $mJ\,m^{-2}$, which is weaker compared to the initial FM coupling estimate. The higher IEC between the RL and PL prevents back-hopping, maintaining stable magnetization orientations throughout the transition. The back-hopping effect, an unintended switching of the magnetic layer in the structure, leads to writing errors in the magnetization state. This stability is crucial for ensuring reliable memory operation, as it minimizes unwanted state changes that can lead to data loss or corruption. This is observed by the magnetization in the graph going to $m_x = -1$, whereas, for the stronger coupling, the magnetization goes to $m_x = 0$, indicating that only the FL switches, as shown in Figs. 3 and 4.

Figs. 2(b) and 2(c) show the initial magnetization set at $m_x = 1$, representing the average magnetization direction of both FL_1 and FL_2, oriented positively along the x-axis, for the structure in Figs. 1(b) and 1(c). In both scenarios, the AFM coupling between the HL and the RL, and the FM coupling between the RL and the PL are kept at -1.5 $mJ\,m^{-2}$ and 0.8 $mJ\,m^{-2}$ respectively.

In Fig. 2(b), a scenario is illustrated with two different ferromagnetic coupling values mediated by the tungsten NMS_W between FL_1 and FL_2. The initial FM connection through NMS_W is proposed at 0.37 $mJ\,m^{-2}$ by Nishioka et al. [44], and the second at 0.8 $mJ\,m^{-2}$ by Chen et al. [45]. For the weaker IEC, the impact is that the coupling is insufficient to keep the two FL parts coupled, leading to separate switching. This results in a plateau at $m_x = 0.5$, where FL_1 starts switching, followed by FL_2, as seen in Fig. 5. In contrast, the performance is slowed down for the higher IEC, but a uniform magnetization reversal is achieved, maintaining a more rigid alignment of the magnetization orientations, as shown in Fig. 6.

Fig. 2(c) presents a configuration with two different ferromagnetic coupling values mediated by the NMS_{Ta} between FL_1 and FL_2. We use the same values as before for the IEC to analyze the performance of the hybrid FL with a Ta spacer. The initial FM connection through NMS_{Ta}

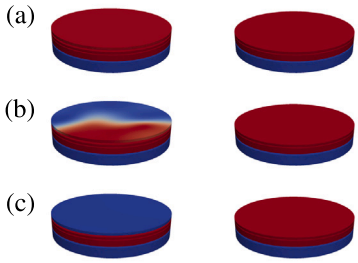

Fig. 3. Magnetization state from P to AP switching in structure Fig. 1(a) with an FM of 0.8 $mJ\,m^{-2}$ between the RL and the PL. (a) initial state at $t = 0$ ns, (b) intermediate phase during reversal at $t = 0.3$ ns, (c) final state at $t = 1$ ns. Left panels: FL_2 (top free layer). Right panels: PL.

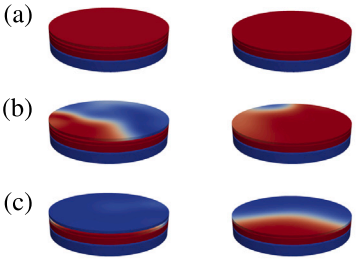

Fig. 4. Magnetization state from P to AP switching in structure Fig. 1(a) with an FM of 0.2 $mJ\,m^{-2}$ between the RL and the PL. (a) initial state at $t = 0$ ns, (b) intermediate state during reversal at $t = 0.3$ ns, (c) intermediate state at $t = 1$ ns. Left panels: FL_2 (top free layer). Right panels: PL.

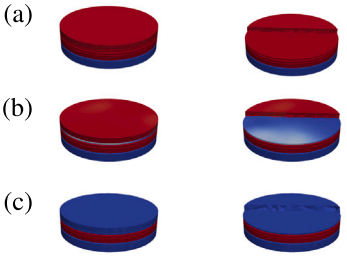

Fig. 5. Magnetization state from P to AP switching in structure Fig. 1(b) with an FM of 0.37 $mJ\,m^{-2}$ between the FLs. (a) initial state at $t = 0$ ns, (b) intermediate phase during reversal at $t = 0.5$ ns, (c) final state at $t = 1.7$ ns. Left panels: FL_2 (top free layer). Right panels: FL_1.

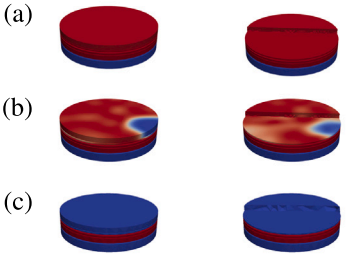

Fig. 6. Magnetization state from P to AP switching in structure Fig. 1(b) with an FM of 0.8 $mJ\,m^{-2}$ between the FLs. (a) initial state at $t = 0$ ns, (b) intermediate phase during reversal at $t = 0.5$ ns, (c) final state at $t = 1.7$ ns. Left panels: FL_2 (top free layer). Right panels: FL_1.

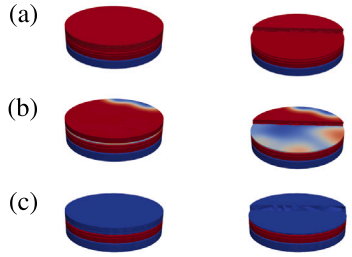

Fig. 7. Magnetization state from P to AP switching in structure Fig. 1(c) with an FM of 0.2 mJ m^{-2} between the FLs. (a) initial state at t = 0 ns, (b) intermediate phase during reversal at t = 0.75 ns, (c) final state at t = 1.7 ns. Left panels: FL_2 (top free layer). Right panels: FL_1.

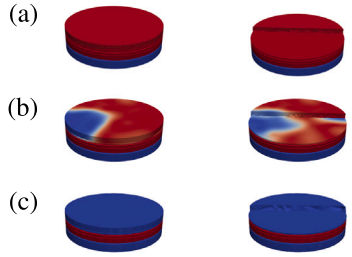

Fig. 8. Magnetization state from P to AP switching in structure Fig. 1(c) with an FM of 0.8 mJ m^{-2} between the FLs. (a) initial state at t = 0 ns, (b) intermediate phase during reversal at t = 0.75 ns, (c) final state at t = 1.7 ns. Left panels: FL_2 (top free layer). Right panels: FL_1.

is proposed at 0.2 mJ m^{-2} by Devolder et al. [42] and Goff et al. [43], and the second at 0.8 mJ m^{-2} by Devolder et al. [41].

In this setup, the stability of the weaker IEC increases. The better stability comes from the weaker torques due to the shorter spin-flip length in the tantalum NMS, resulting in the absence of the plateau at $m_x = 0.5$ during the magnetization reversal seen in Fig. 2(b). Like before, the stronger coupling forces the layers to align more rigidly, decreasing the performance. Furthermore, the overall less efficient performance is attributed to the shorter spin-flip length λ_{sf}. As the FL_2 inverts its magnetization, we obtain a similar configuration as in double spin-torque MTJs, where a longer λ_{sf} increases the torques. The λ_{sf} for tungsten is 2.4 nm, compared to 1.9 nm for tantalum [46]. We employ Ta and W as spacers for practical reasons, not merely for comparison: both are fabrication-friendly heavy-metal layers in CoFeB/MgO stacks that act as boron sinks during annealing, promote CoFeB crystallization, preserve high TMR, and serve as diffusion barriers compatible with CMOS backend thermal budgets [47–49]. W underlayers/caps often sustain perpendicular anisotropy to higher anneal temperatures than Ta, accordingly, W is preferred for aggressive anneals, whereas Ta remains effective within standard backend thermal budgets [50–52]. We note the expected role of the damping constant α. Increasing α raises the critical switching current/voltage (proportional in the macrospin limit [38]), suppresses precession, and makes the intermediate plateau near $m_x \approx 0.5$ more persistent at fixed bias, often requiring longer pulses for reversal. Decreasing α has the opposite effect: lower critical current, enhanced precessional overshoot, and a tendency to remove that transient plateau. In this study, α is fixed, so our conclusions for weaker versus stronger IEC and for Ta versus W are unaffected by variations in α. Interfaces are modeled as ideal, atomically flat FM/MgO boundaries, morphological roughness and spin-memory-loss effects are not included and would only enter via modified effective parameters.

The sequential switching behavior observed in Figs. 5 and 7 is a direct consequence of the distribution of STT across the multilayer structure. The torque calculations indicate that the dominant STT is concentrated at the PL|TB and TB|FL_1 interface, while the torque at NMS_W is negligible. As a result, FL_1 experiences a significantly stronger torque, reaching its critical switching threshold first. In contrast, FL_2 remains in its initial state longer, as it is not directly affected by a substantial STT at the NMS_W interface.

Once FL_1 switches, the system enters an intermediate state where the magnetizations of FL_1 and FL_2 are misaligned, leading to an increase in IEC. The rise of IEC, combined with spin accumulation effects from switching FL_1, eventually allows FL_2 to reverse, completing the transition to the AP configuration. This results in a two-step switching process rather than a simultaneous transition of both free layers.

For stronger IEC in Figs. 6 and 8, the rigid coupling between FL_1 and FL_2 prevents the independent switching, leading to a more synchronized magnetization reversal. However, this comes at the cost of reduced switching speed, as the coupling constrains the dynamics of each layer and increases the overall energy required for the transition. In the weaker IEC case, the increased flexibility allows FL_1 to switch first, improving the switching speed but leading to a transient misalignment between the two free layers.

These results highlight the fundamental role of the IEC strength and STT distribution in governing the switching dynamics of STT-MRAM. By optimizing these parameters, it is possible to balance switching efficiency and stability for specific spintronic applications.

Fig. 9 presents the spin-torque calculations during the transition from the P to AP configuration, offering a detailed visualization of how STT components influence different regions of the structure. To gain a more comprehensive understanding of the switching process, we have decomposed the transition into four stages, allowing us to track the evolution of damping-like ($T_{S,z}$) and field-like ($T_{S,x}$) torques throughout the structure. This breakdown provides deeper insight into how these torques develop over time and drive the magnetization dynamics of each layer. Furthermore, as previously discussed, in dynamic micromagnetics, expressing all energy terms as effective fields rather than through boundary conditions facilitates seamless integration into the LLG equation, while also allowing for isolating the pure torque contribution, which remains unaffected by IEC.

Panels (a–d) in Fig. 9 illustrate the spin-torque distribution in the structure from Fig. 1(a). In this configuration, the system initially exhibits back-hopping, where the magnetization begins to switch but partially reverses before stabilizing in the final AP state. This behavior results from the weaker IEC between the RL and the PL, allowing independent motion of magnetic layers and preventing a stable transition.

Panel (a) represents the initial P configuration, with the FL tilted by five degrees in the z-direction. At this stage, torques from both the RL and FL stabilize the PL, while the torques from the PL initiate the switching process in the FL. The $T_{S,z}$ drives the magnetization along the z-direction, beginning the transition towards the AP state. In panel (b), as the magnetization progresses, reaching a 45-degree angle, the $T_{S,x}$ increases, further driving the magnetization toward the AP configuration. Simultaneously, $T_{S,z}$ in the PL rises, attempting to destabilize the P configuration and overcome the initial alignment. By Panel (c), as the magnetization reaches 135 degrees, the torques in both the PL and FL increase by an order of magnitude, significantly accelerating the transition. At this stage, the FL is pushed towards the AP configuration, but the PL becomes destabilized, making it susceptible to reversal. If the IEC between the RL and the PL is weak, as depicted in Fig. 2(a), the applied torques become sufficient to overcome the IEC, leading to back-hopping in the PL. Panel (d) illustrates the final stage, where the PL magnetization approaches the AP configuration. At this point, the remaining torque drives the PL magnetization entirely into the AP state, reflected in Fig. 2(a) as a plateau at $m_x = 0$. This plateau signifies the transient misalignment due to PL reversal, further confirming the instability caused by weak IEC. This instability arises because the reduced IEC allows independent motion of the magnetic layers, preventing a fully synchronized transition. The $T_{S,z}$ primarily

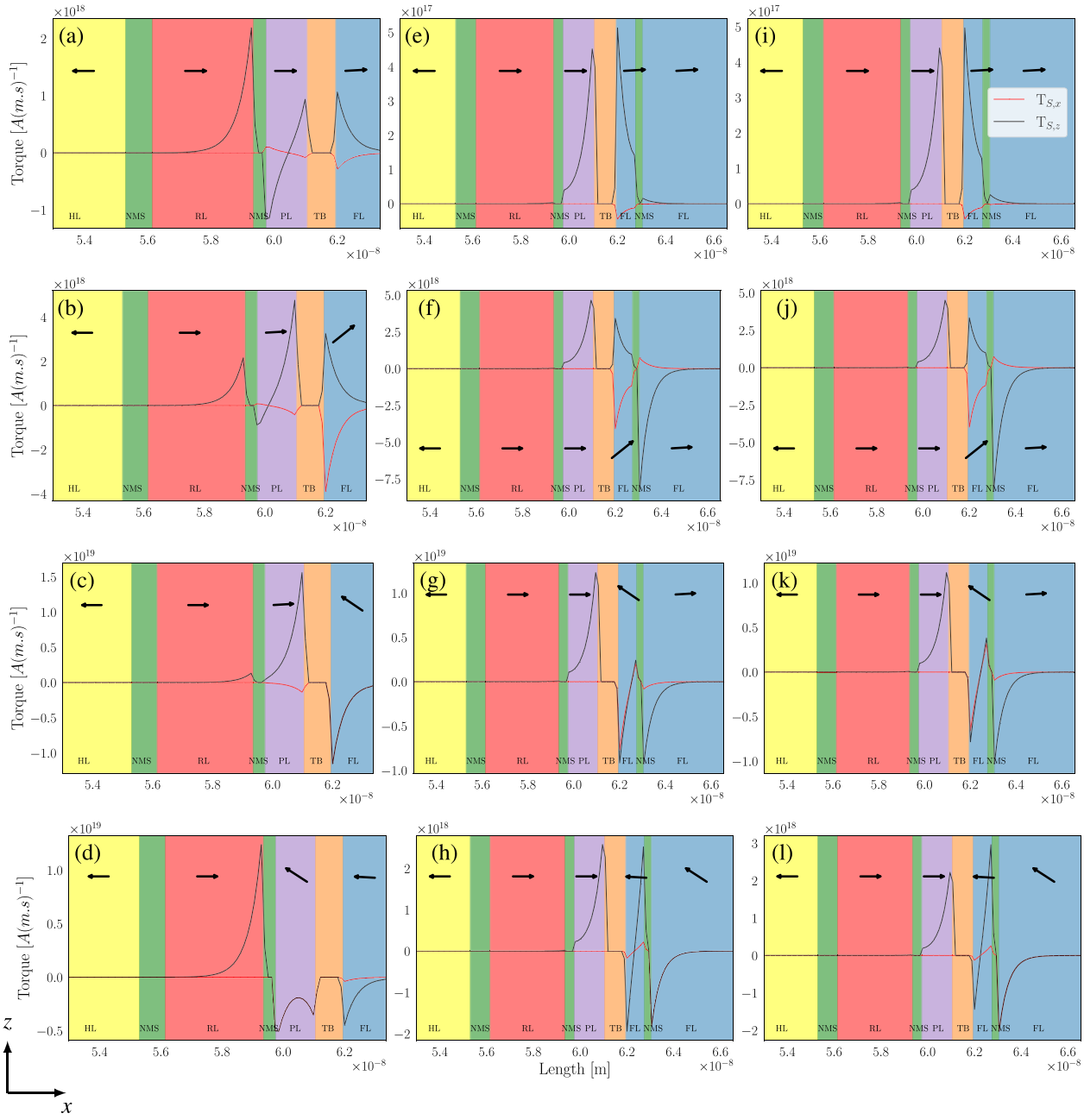

Fig. 9. The spin torque applied to three different configurations: (a–d) structure Fig. 1(a), (e–h) structure Fig. 1(b), and (i–l) structure Fig. 1(c), respectively. These figures demonstrate the torque patterns as the magnetization reaches the final AP configuration when traversing from P to AP. In these diagrams, the direction of the magnetization in the ferromagnetic sections is indicated by black arrows. The graphical representation reveals that $T_{S,x}$ acts as a field-like component of the spin torque along the central axis of the structure, whereas $T_{S,z}$ serves as a damping-like component.

acts on the PL, attempting to reverse its magnetization. However, when the RL and the PL are strongly coupled, this reversal can be suppressed, leading to a more rigid and stable magnetization alignment of the SAF-layer, which prevents back-hopping.

Panels (e–h) in Fig. 9 illustrate the spin-torque distribution in the structure from Fig. 1(b). Like in the previous case, Panel (e) represents the initial P configuration, with both FLs tilted by five degrees in z-direction. As discussed earlier, the sequential switching behavior observed in Fig. 5 and also visible in Fig. 2(b), characterized by a quicker response and a plateau at $m_x = 0.5$, is a direct consequence of the STT distribution across the multilayer structure. In this configuration, the $T_{S,z}$ influences both the PL and FL_1, simultaneously driving their switching processes, while the $T_{S,x}$ introduces additional precessional motion along the central axis. However, while the IEC through the NMS effectively maintains alignment with the RL, the IEC between FL_1 and FL_2 is weaker, allowing FL_1 to initiate switching before FL_2. Panel (f) illustrates the progression of FL_1 magnetization toward the AP configuration. As the switching process advances, $T_{S,x}$ and $T_{S,z}$ increase, further driving FL1 toward reversal. At the same time, TS, z stabilizes FL_2, temporarily holding it in its initial state. In Panel (g), once FL_1 approaches the AP configuration, the torques increase by an order of magnitude, completing the full magnetization reversal of FL_1. Meanwhile, $T_{S,z}$ in FL_2 begins destabilizing its magnetization, initiating its transition toward the AP state. Panel (h) illustrates the final stage, where FL_2 magnetization approaches the AP configuration. At this point, the remaining torque drives FL_2 into the AP state,

completing the sequential switching process. This behavior highlights the interplay between STT and IEC, where a strong IEC promotes synchronized switching, while a weaker IEC allows FL_1 to switch freely before FL_2 completes its transition. The stepwise reversal process seen in this structure confirms the role of interlayer coupling in determining switching order and stability in STT-driven magnetization dynamics.

Panels (i–l) in Fig. 9 illustrate the spin-torque distribution in the structure from Fig. 1(c), which exhibits a similar torque distribution to the previous case but with a weaker damping-like component. This reduction in torque strength is directly attributed to the shorter spin-flip length in the NMS separating the FLs [46], which reduces the efficiency of spin transfer and weakens the STT-driven switching process. As a result, the sequential switching observed in Fig. 7 differs slightly from that in Fig. 5. Here, the switching of FL_1 is less pronounced, reversing more gradually before FL_2 follows. This behavior is further supported by the weaker STT at the NMS_{Ta} interface, also evident in Fig. 2(c) through the absence of the pronounced plateau at $m_x = 0.5$. This indicates that direct STT does not immediately influence FL_2, but switches due to accumulated spin effects from FL_1, reinforcing the stepwise magnetization reversal. The most significant distinction in torque behavior can be observed by comparing Panel (h) and Panel (l). In Panel (l), the system approaches a configuration similar to that in double-spin-torque MTJs, where the torques are redistributed across the structure, further confirming the differences in switching dynamics due to the choice of NMS material and its spin transport properties.

For completeness, we report the write efficiency,

$$\eta_{\mathrm{write}} \equiv \frac{\Delta}{I_{c0}}, \qquad \Delta = \frac{E_b}{k_B T}.$$

With perpendicular anisotropy, the energy barrier for switching one layer can be written as

$$E_b \approx K_{\mathrm{eff}} V \pm J A,$$

and in the macrospin approximation, the zero-temperature critical current is

$$I_{c0} \approx \frac{2e\alpha M_s V}{\hbar \eta}\left(H_k \pm H_{\mathrm{IEC}}\right), \qquad H_{\mathrm{IEC}} = \frac{J}{\mu_0 M_s t}.$$

Here, η_{write} is the write-efficiency index, Δ is the thermal stability factor, E_b is the energy barrier, k_B is the Boltzmann constant, T is the absolute temperature, K_{eff} is the effective perpendicular anisotropy energy density, V is the magnetic volume of the switching layer, J is the interlayer-exchange coupling energy density, A is the interface area, I_{c0} is the zero-temperature critical current, e is the elementary charge, α is the Gilbert damping constant, M_s is the saturation magnetization, $\hbar$ is the reduced Planck constant, η is the spin-transfer efficiency (spin polarization factor), H_k is the effective anisotropy field, μ_0 is the vacuum permeability, and t is the thickness of the layer being switched. When IEC is introduced as a boundary energy $E_{\mathrm{IEC}} = -J\,\mathbf{m}_i \cdot \mathbf{m}_j$, $\mathbf{m}_i$ and $\mathbf{m}_j$ denote the unit magnetization vectors of the adjacent layers at the interface, the variational torque from this surface term is analytically equivalent to the "coupling field" H_{IEC} used here for scaling arguments.

Applied to our stacks, Fig. 2(a) has nearly symmetric layer thicknesses (PL ≈ 1.3 nm, FL ≈ 1.4 nm), so the J–dependent terms in E_b and I_{c0} co-modulate and largely cancel in η_{write}, making write efficiency only weakly sensitive to IEC. In Fig. 2(b)–(c) the free layers are asymmetric (FL_2 = 3.5 nm, FL_1 = 0.8 nm); because $H_{\mathrm{IEC}} = J/(\mu_0 M_s t)$, the thicker FL_2 experiences a smaller coupling field than the thinner FL_1, so the cancellation is incomplete. Consistent with our bias trends in Figs. 3–8, weaker coupling reduces I_{c0} more than it reduces E_b, yielding a modest increase in η_{write}, whereas stronger coupling raises both stability and required current at comparable rates and leaves η_{write} nearly unchanged.

Overall, this analysis underscores the critical role of IEC strength and STT distribution in determining the switching dynamics of STT-MRAM. Effective control over these interactions is essential for minimizing back-hopping, enhancing switching efficiency, and improving the reliability of STT-MRAM devices.

3. Conclusion

Our study highlights the critical role of IEC in enhancing magnetic stability and optimizing STT switching efficiency in multilayered STT-MRAM, including SAF structures. By carefully tuning IEC, we can significantly improve data retention, reduce write/read times, and enhance overall device reliability, all of which are crucial for overcoming the challenges posed by device miniaturization in modern spintronic memory applications.

Furthermore, our findings emphasize the fundamental influence of spacer properties on IEC strength and switching behavior. Variations in spacer materials directly impact coupling energy and magnetic orientation stability, offering insights into designing more efficient and reliable STT-MRAM devices. The spin-torque calculations presented in this work provide a detailed view of how damping-like and field-like torques contribute to magnetization reversal, reinforcing the importance of precise IEC control to minimize back-hopping and improve switching consistency.

CRediT authorship contribution statement

M. Bendra: Conceptualization, Methodology, Software, Validation, Formal analysis, Investigation, Data curation, Writing – original draft, Writing – review & editing, Visualization. **W. Goes:** Resources, Writing – review & editing, Supervision. **S. Selberherr:** Resources, Writing – review & editing, Supervision, Funding acquisition. **V. Sverdlov:** Conceptualization, Methodology, Validation, Writing – review & editing, Supervision, Project administration, Funding acquisition.

Declaration of competing interest

The authors declare the following financial interests/personal relationships which may be considered as potential competing interests: Mario Bendra reports a relationship with TU Wien Library that includes: funding grants. Mario Bendra reports a relationship with Christian Doppler Research Association that includes: funding grants. Mario Bendra reports a relationship with TU Wien Institute for Microelectronics that includes: employment. If there are other authors, they declare that they have no known competing financial interests or personal relationships that could have appeared to influence the work reported in this paper.

Acknowledgments

The financial support by the Federal Ministry of Labour and Economy, the National Foundation for Research, Technology, and Development, the Christian Doppler Research Association, and the TU Wien Library for financial support through its Open Access Funding Program is gratefully acknowledged.

All authors have read and agreed to the published version of the manuscript.

Data availability

Data will be made available on request.

References

[1] N. Lepri, A. Glukhov, L. Cattaneo, M. Farronato, P. Mannocci, et al., In-Memory Computing for Machine Learning and Deep Learning, IEEE J. Electron Devices Soc. 11 (2023) 587–601, http://dx.doi.org/10.1109/JEDS.2023.3265875.

[2] S. Jung, H. Lee, S. Myung, H. Kim, S.K. Yoon, et al., A Crossbar Array of Magnetoresistive Memory Devices for In-Memory Computing, Nature 601 (2022) 211–216, http://dx.doi.org/10.1038/s41586-021-04196-6.

[3] J.A.C. Incorvia, T.P. Xiao, N. Zogbi, et al., Spintronics for Achieving System-Level Energy-Efficient Logic, Nat. Rev. Electr. Eng. 1 (2024) 700–713, http://dx.doi.org/10.1038/s44287-024-00103-z.

[4] V.B. Naik, K. Yamane, T. Lee, J. Kwon, R. Chao, et al., JEDEC-Qualified Highly Reliable 22nm FD-SOI Embedded MRAM For Low-Power Industrial-Grade, and Extended Performance Towards Automotive-Grade-1 Applications, in: IEEE International Electron Devices Meeting, IEDM, 2020, pp. 11.3.1–11.3.4, http://dx.doi.org/10.1109/IEDM13553.2020.9371935.

[5] K. Roy, C. Wang, S. Roy, et al., Spintronic Neural Systems, Nat. Rev. Electr. Eng. 1 (2024) 714–729, http://dx.doi.org/10.1038/s44287-024-00107-9.

[6] S. Ikegawa, K. Nagel, F.B. Mancoff, S.M. Alam, M. Arora, et al., High-Speed (400MB/s) and Low-BER STT-MRAM Technology for Industrial Applications, in: IEEE International Electron Devices Meeting, IEDM, 2022, pp. 10.4.1–10.4.4, http://dx.doi.org/10.1109/IEDM45625.2022.10019513.

[7] K. Cai, T. Jin, W.S. Lew, Spin-Based Magnetic Random-Access Memory for High-Performance Computing, Natl. Sci. Rev. 11 (3) (2023) nwad272, http://dx.doi.org/10.1093/nsr/nwad272.

[8] C.H. Marrows, J. Barker, T.A. Moore, et al., Neuromorphic Computing with Spintronics, Npj Spintron. 2 (2024) 12, http://dx.doi.org/10.1038/s44306-024-00019-2.

[9] K.-F. Lin, H. Noguchi, Y.-C. Shih, P.-F. Yuh, Y.-J. Lee, et al., 15.9 A 16nm 16Mb Embedded STT-MRAM with a 20ns Write Time, a 1012 Write Endurance and Integrated Margin-Expansion Schemes, ISSCC, in: 2024 IEEE International Solid-State Circuits Conference, vol. 67, 2024, pp. 292–294, http://dx.doi.org/10.1109/ISSCC49657.2024.10454339.

[10] B. Jinnai, J. Igarashi, K. Watanabe, T. Funatsu, H. Sato, et al., High-Performance Shape-Anisotropy Magnetic Tunnel Junctions Down to 2.3 nm, in: IEEE International Electron Devices Meeting, IEDM, 2020, pp. 24.6.1–24.6.4, http://dx.doi.org/10.1109/IEDM13553.2020.9371972.

[11] K. Nishioka, H. Honjo, S. Ikeda, T. Watanabe, S. Miura, et al., Novel Quad Interface MTJ Technology and its First Demonstration with High Thermal Stability and Switching Efficiency for STT-MRAM Beyond 2Xnm, in: Symposium on VLSI Technology, 2019, pp. T120–T121, http://dx.doi.org/10.23919/VLSIT.2019.8776499.

[12] M. Bendra, W. Goes, S. Selberherr, V. Sverdlov, Simulation of SAF-Enhanced Multilayered STT-MRAM Structures, in: 2024 Austrochip Workshop on Microelectronics (Austrochip), 2024, pp. 1–4, http://dx.doi.org/10.1109/Austrochip62761.2024.10716241.

[13] R. Phoomatna, S. Sampan-a pai, A. Meo, R.W. Chantrell, J. Chureemart, et al., Dimensional Scaling Effects on Critical Current Density and Magnetization Switching in CoFeB-Based Magnetic Tunnel Junction, J. Phys. D: Appl. Phys. 57 (18) (2024) 185002, http://dx.doi.org/10.1088/1361-6463/ad2477.

[14] C. Abert, H. Sepehri-Amin, F. Bruckner, C. Vogler, M. Hayashi, et al., Back-Hopping in Spin-Transfer-Torque Devices: Possible Origin and Countermeasures, Phys. Rev. Appl. 9 (2018) 054010, http://dx.doi.org/10.1103/PhysRevApplied.9.054010.

[15] S.-M. Ahn, Antiferromagnetically Coupled CoFe/MgO/CoFe Stacks, Phys. Scr. 98 (10) (2023) 105948, http://dx.doi.org/10.1088/1402-4896/acf80f.

[16] M.K. Yadav, R. Kumar, R.K. Ratnesh, J. Singh, R. Chandra, et al., Revolutionizing Technology with Spintronics: Devices and Their Transformative Applications, Mater. Sci. Eng.: B 303 (2024) 117293, http://dx.doi.org/10.1016/j.mseb.2024.117293.

[17] E. Garzón, M. Lanuzza, A. Teman, L. Yavits, AM4: MRAM Crossbar Based CAM/TCAM/ACAM/AP for In-Memory Computing, IEEE J. Emerg. Sel. Top. Circuits Syst. 13 (1) (2023) 408–421, http://dx.doi.org/10.1109/JETCAS.2023.3243222.

[18] S. Ikegawa, K. Nagel, M. DeHerrera, F.B. Mancoff, H.K. Lee, et al., Discrete STT-MRAM Products for Industrial and Automotive Markets, in: 2024 IEEE 35th Magnetic Recording Conference, TMRC, 2024, pp. 1–2, http://dx.doi.org/10.1109/TMRC62973.2024.10713976.

[19] H. Sato, M. Yamanouchi, S. Ikeda, S. Fukami, F. Matsukura, et al., MgO/CoFeB/Ta/CoFeB/MgO Recording Structure in Magnetic Tunnel Junctions With Perpendicular Easy Axis, TMAG, in: IEEE Transactions on Magnetics, vol. 49, 2013, pp. 4437–4440, http://dx.doi.org/10.1109/TMAG.2013.2251326.

[20] T. Shinoda, J. Igarashi, B. Jinnai, S. Fukami, H. Ohno, Pitch Scaling Prospect of Ultra-Small Magnetic Tunnel Junctions for High-Density STT-MRAM: Effects of Magnetostatic Interference From Neighboring Bits, IEEE Electron Device Lett. 45 (2) (2024) 184–187, http://dx.doi.org/10.1109/LED.2023.3345743.

[21] H. Naganuma, Spintronics Memory Using Magnetic Tunnel Junction for X nm-Generation, Japan. J. Appl. Phys. 62 (SG) (2023) SG0811, http://dx.doi.org/10.35848/1347-4065/accaed.

[22] D. Zeng, F. Meng, R. Chen, Y. Gao, Y. Sun, et al., Achieving Over 95% Yield of Sub-1ppm BER With Retention Over 10 Years at 125 ° C and Endurance of 1E12 Cycles Towards Automotive Non-Volatile RAM Applications, J. Semicond. 46 (1) (2025) 1–6, http://dx.doi.org/10.1088/1674-4926/24090037.

[23] S. Fiorentini, M. Bendra, J. Ender, R.L. de Orio, W. Goes, et al., Spin and Charge Drift-Diffusion in Ultra-Scaled MRAM Cells, Sci. Rep. 12 (2022) 20958, http://dx.doi.org/10.1038/s41598-022-25586-4.

[24] J. Ender, M. Mohamedou, S. Fiorentini, R. Orio, S. Selberherr, W. Goes, V. Sverdlov, Efficient demagnetizing field calculation for disconnected complex geometries in STT-MRAM cells, in: 2020 International Conference on Simulation of Semiconductor Processes and Devices, SISPAD, 2020, pp. 213–216, http://dx.doi.org/10.23919/SISPAD49475.2020.9241662.

[25] M.A. Ruderman, C. Kittel, Indirect Exchange Coupling of Nuclear Magnetic Moments by Conduction Electrons, Phys. Rev. 96 (1954) 99–102, http://dx.doi.org/10.1103/PhysRev.96.99.

[26] T. Kasuya, A Theory of Metallic Ferro- and Antiferromagnetism on Zener's Model, Progr. Theoret. Phys. 16 (1) (1956) 45–57, http://dx.doi.org/10.1143/PTP.16.45.

[27] K. Yosida, Magnetic Properties of Cu-Mn Alloys, Phys. Rev. 106 (1957) 893–898, http://dx.doi.org/10.1103/PhysRev.106.893.

[28] M. Bendra, R.L.d. Orio, S. Selberherr, W. Goes, V. Sverdlov, Advanced Modeling and Simulation of Multilayer Spin–Transfer Torque Magnetoresistive Random Access Memory with Interface Exchange Coupling, Micromachines 15 (5) (2024) http://dx.doi.org/10.3390/mi15050568.

[29] H. Naganuma, H. Honjo, C. Kaneta, K. Nishioka, S. Ikeda, T. Endoh, Micromagnetic simulation of the temperature dependence of the switching energy barrier using string method assuming sidewall damages in perpendicular magnetized magnetic tunnel junctions, AIP Adv. 10 (7) (2020) 075106, http://dx.doi.org/10.1063/5.0007499.

[30] T. Kolev, V. Dobrev, MFEM: Modular finite element methods library, 2024, http://mfem.org. (Accessed 24 March 2024).

[31] ViennaSpinMag, An Open Access Finite Element-based Application for Calculating the Magnetization Dynamics of Multi-Layered Structures Composed of Ferromagnets, Metal Spacers and Tunnel Barriers., 2024, https://www.iue.tuwien.ac.at/viennaspinmag/. (Accessed 24 March 2024).

[32] A. Mouhoub, F. Millo, C. Chappert, J.-V. Kim, J. Létang, et al., Exchange Energies in CoFeB/Ru/CoFeB Synthetic Antiferromagnets, Phys. Rev. Mater. 7 (2023) 044404, http://dx.doi.org/10.1103/PhysRevMaterials.7.044404.

[33] M. Wang, W. Cai, K. Cao, J. Zhou, J. Wrona, et al., Current-induced magnetization switching in atom-thick tungsten engineered perpendicular magnetic tunnel junctions with large tunnel magnetoresistance, Nat. Commun. 9 (2018) 671, http://dx.doi.org/10.1038/s41467-018-03140-z.

[34] M. Wang, Tunnel junction with perpendicular magnetic anisotropy: Status and challenges, Micromachines 6 (8) (2015) 1023–1045, http://dx.doi.org/10.3390/mi6081023.

[35] J.M. Iwata-Harms, et al., Ultrathin perpendicular magnetic anisotropy CoFeB free layers for highly efficient, high speed writing in spin-transfer-torque MRAM, Sci. Rep. 9 (2019) 18668, http://dx.doi.org/10.1038/s41598-019-54466-7.

[36] A.A. Timopheev, et al., Second order anisotropy contribution in perpendicular magnetic tunnel junctions, Sci. Rep. 6 (2016) 26877, http://dx.doi.org/10.1038/srep26877.

[37] Y. Shao, et al., Sub-volt switching of nanoscale voltage-controlled perpendicular magnetic tunnel junctions, Commun. Mater. 3 (1) (2022) 30, http://dx.doi.org/10.1038/s43246-022-00310-x.

[38] J.Z. Sun, Spin-current interaction with a monodomain magnetic body: A model study, Phys. Rev. B 62 (1) (2000) 570–578, http://dx.doi.org/10.1103/PhysRevB.62.570.

[39] T. Devolder, A. Le Goff, V. Nikitin, Size dependence of nanosecond-scale spin-torque switching in perpendicularly magnetized tunnel junctions, Phys. Rev. B 93 (2016) 224432, http://dx.doi.org/10.1103/PhysRevB.93.224432.

[40] S. Lepadatu, Boris computational spintronics online materials database, 2024, http://www.boris-spintronics.uk/online-materials-database/. (Accessed 24 March 2024).

[41] T. Devolder, J.-V. Kim, F. Garcia-Sanchez, J. Swerts, W. Kim, et al., Time-Resolved Spin-Torque Switching in MgO-Based Perpendicularly Magnetized Tunnel Junctions, Phys. Rev. B 93 (2016) 024420, http://dx.doi.org/10.1103/PhysRevB.93.024420.

[42] T. Devolder, O. Bultynck, P. Bouquin, V.D. Nguyen, S. Rao, et al., Back Hopping in Spin Transfer Torque Switching of Perpendicularly Magnetized Tunnel Junctions, Phys. Rev. B 102 (2020) 184406, http://dx.doi.org/10.1103/PhysRevB.102.184406.

[43] A. Le Goff, K. Garcia, N. Vernier, T. Tahmasebi, S. Cornelissen, et al., Effect of Ta Insertion in Reference Layers of MTJs With Perpendicular Anisotropy, IEEE Trans. Magn. 50 (11) (2014) 1–4, http://dx.doi.org/10.1109/TMAG.2014.2328664.

[44] K. Nishioka, H. Honjo, H. Naganuma, T.V.A. Nguyen, M. Yasuhira, et al., Enhancement of Magnetic Coupling and Magnetic Anisotropy in MTJs with Multiple CoFeB/MgO Interfaces for High Thermal Stability, AIP Adv. 11 (2) (2021) 025231, http://dx.doi.org/10.1063/9.0000048.

[45] J. Chen, S. Peng, D. Xiong, H. Cheng, H. Zhou, et al., Correlation of Interfacial Perpendicular Magnetic Anisotropy and Interlayer Exchange Coupling in CoFe/W/CoFe Structures, J. Phys. D: Appl. Phys. 53 (33) (2020) 334001, http://dx.doi.org/10.1088/1361-6463/ab8bfe.

[46] B. Pruckner, S. Fiorentini, W. Goes, S. Selberherr, V. Sverdlov, Micromagnetic Modeling of Double Spin-Torque Magnetic Tunnel Junction Devices, Phys. B 688 (2024) 416124, http://dx.doi.org/10.1016/j.physb.2024.416124.

[47] G. Kim, S. Lee, S. Lee, B. Song, B.-K. Lee, D. Lee, J.S. Lee, M.H. Lee, Y.K. Kim, B.-G. Park, The influence of capping layers on tunneling magnetoresistance and microstructure in CoFeB/MgO/CoFeB magnetic tunnel junctions upon annealing, Nanomaterials 13 (18) (2023) 2591, http://dx.doi.org/10.3390/nano13182591.

[48] H. Bouchikhaoui, P. Stender, Z. Balogh-Michels, D. Baither, A. Hütten, K. Hono, G. Schmitz, Nano-analysis of Ta/FeCoB/MgO tunnel magnetoresistance structures, Acta Mater. 116 (2016) 298–307, http://dx.doi.org/10.1016/j.actamat.2016.06.045.

[49] S. Mukherjee, R. Knut, S.M. Mohseni, T.N.A. Nguyen, S. Chung, Q.T. Le, J. Åkerman, J. Persson, A. Sahoo, A. Hazarika, B. Pal, S. Thiess, M. Gorgoi, P.S. Anil Kumar, W. Drube, O. Karis, D.D. Sarma, Role of boron diffusion in CoFeB/MgO magnetic tunnel junctions, Phys. Rev. B 91 (8) (2015) 085311, http://dx.doi.org/10.1103/PhysRevB.91.085311.

[50] G.G. An, J.B. Lee, S.M. Yang, J.H. Kim, W. Chung, J. Hong, Highly stable perpendicular magnetic anisotropies of CoFeB/MgO frames employing w buffer and capping layers, Acta Mater. 87 (2015) 259–265, http://dx.doi.org/10.1016/j.actamat.2015.01.022.

[51] W. Skowroński, T. Nozaki, D.D. Lam, Y. Shiota, K. Yakushiji, H. Kubota, A. Fukushima, S. Yuasa, Y. Suzuki, Underlayer material influence on electric-field controlled perpendicular magnetic anisotropy in CoFeB/MgO magnetic tunnel junctions, Phys. Rev. B 91 (2015) 184410, http://dx.doi.org/10.1103/PhysRevB.91.184410.

[52] Y.Q. Guo, H. Bai, Q.R. Cui, L.M. Wang, Y.C. Zhao, X.Z. Zhan, T. Zhu, H.X. Yang, Y. Gao, C.Q. Hu, S.P. Shen, C.L. He, S.G. Wang, High thermal stability of perpendicular magnetic anisotropy in the MgO/CoFeB/W thin films, Appl. Surf. Sci. 568 (2021) 150857, http://dx.doi.org/10.1016/j.apsusc.2021.150857.